Comparisons between Polarimetric Radio Occultation Measurements with WRF Model Simulation for Tropical Cyclones

Shu-Ya Chen[1], Ying-Hwa Kuo[2], Hsiu-Wen Li[1], Ramon Padullés[3], Estel Cardellach[3], F. Joseph Turk[4]

[1]GPS Science and Application Research Center, National Central University, Taiwan
5 [2]UCAR Community Programs, University Corporation for Atmospheric Research, USA
[3]Institute of Space Sciences (ICE-CSIC), Institute of Space Studies of Catalonia (IEEC), Spain
[4]Jet Propulsion Laboratory, California Institute of Technology, USA

Correspondence to: Shu-Ya Chen (shuyachen@ncu.edu.tw)

10 **Abstract.** A novel radio occultation (RO) technique, polarimetric RO (PRO), has recently been developed to measure differential polarimetric phase shift together with traditional RO products such as temperature and moisture. PRO observations have been shown to be associated with the vertical structure of cloud hydrometeors. With this unique measurement capability, the PRO soundings could potentially be used to evaluate model microphysics. This study compared PRO observations with WRF simulations of three typhoon cases in 2019 and 2021, initialized with ERA5 and NCEP FNL global analysis, respectively,
15 with five microphysics parameterizations (Purdue Lin, WSM6, Goddard, Thompson, and Morrison). There is notable variability in the distribution of the model's hydrometeors, which could be affected by the initial conditions, microphysics parameterization schemes, typhoon locations, and circulation rainbands. The results show that WRF simulation initialized with ERA5 and using the Goddard microphysics scheme performs better in synoptic-scale verification and comparisons with PRO observations. The ensemble mean from 36 ensemble forecasts also exhibits consistent results with the deterministic run. The
20 comparative results demonstrate that PRO data have the potential to evaluate the performance of different microphysics schemes in numerical models.

1 Introduction

The Global Navigation Satellite System (GNSS) radio occultation (RO) technique detects the phase delay induced by the atmospheric variation of air density and water vapor. This has been demonstrated by providing useful observations for climate
25 monitoring and numerical weather prediction, e.g., Anthes (2011), Gleisner et al. (2020, 2022), and Ho et al. (2020). The RO data provide profiles of atmospheric bending angle and refractivity with high accuracy and precision, as well as global coverage. These RO products can assist in understanding the atmospheric thermodynamic process (e.g., Chen et al., 2020, 2021; Chang and Yang, 2022; Hong et al., 2023), and the data have been routinely assimilated for operational weather prediction (e.g., Cucurull, 2023; Lien et al., 2021; Ruston and Healy, 2020). In recent years, a novel technique known as
30 polarimetric radio occultation (PRO) has been introduced (Cardellach et al., 2015). This technique is similar to the traditional

RO method but employs a dual-polarization RO receiver, which acquires GNSS signals in both horizontal and vertical polarizations. The polarized horizontal and vertical signals passing through atmospheric hydrometeors result in different phase delays due to the shape of hydrometeors. By analyzing the differential polarimetric phase shift (i.e., phase delay of the horizontally polarized signal with respect to the vertically polarized one), we can gain a better understanding of the structure
35   and composition of cloud hydrometeors. The PRO data can provide not only traditional atmospheric thermodynamic profiles of temperature and moisture but also relevant information about atmospheric precipitation in the cloud (Cardellach et al., 2017).

The Spanish PAZ satellite was successfully launched in February 2018 and began operations in May of the same year (Cardellach et al., 2019). Since then, the PAZ Radio Occultations through Heavy Precipitation (ROHP) receiver payload has
40   provided about 200 PRO soundings daily around the globe. Starting in 2023, more PRO data have been available from the commercial company Spire Global (Talpe et al., 2024; Padullés et al., 2024), which has acquired over 2,000 PRO profiles per day during some periods. With abundant sounding observations, it starts to be feasible to envisage PRO applications for monitoring the atmospheric environment, for use in numerical models, and to better characterize the link between thermodynamics and intense precipitation in the atmosphere (Turk et al., 2024). Several studies have substantiated the PAZ
45   satellite's capability of sensing precipitation. Cardellach et al. (2019) and Padullés et al. (2020) validated the PRO data against the joint NASA/JAXA Global Precipitation Measurement (GPM) mission, Integrated Multi-satellitE Retrievals for GPM (IMERG) global precipitation dataset, showing a high correlation between the differential phase shift from PAZ PRO and satellite measurements of precipitation, not only in the lower troposphere but also for frozen particles above the freezing level. Padullés et al. (2022) complemented the validation with data from the GPM Microwave Imager (GMI), the GPM Dual
50   Frequency Precipitation Radar (DPR) and the W-band Cloudsat radar, demonstrating the sensitivity to the vertical extent of the ice hydrometeors above the freezing level. Murphy et al. (2019) used airborne synthetic PRO data to compare with numerical simulations for an intense atmospheric river event. The simulated differential polarimetric phase shifts from the Weather Research and Forecasting (WRF) model with two model microphysics schemes showed significant differences, with differences larger than the PRO noise level (thus detectable by this technique). These results suggest the potential of PRO data
55   for validating model microphysics representation.

With climate change, severe weather events, such as intense typhoons, accompanied by extreme precipitation have been increasing (Tabari, 2020; Masson-Delmotte et al., 2021), which demands more accurate precipitation forecast. However, the prediction of precipitation is associated with the cloud microphysical parameterization of a numerical model. Currently, the microphysical processes in most of the weather and climate models are represented as bulk microphysics parameterizations
60   without a lot of details (such as the hydrometeor size distribution); therefore, the evaluation of these parameterizations has been a challenge. Hristova-Veleva et al. (2021) evaluated WRF simulations with different microphysical parameters against multi-parameter satellite data and their analyses revealed significant differences that highlighted the uncertainty in model microphysics parameterization. This highlights the need for more studies to evaluate the cloud microphysical parameterization and to gain further insights on the microphysical processes.

65   There are a few types of satellite remote sensing observations for precipitation. Satellite radiance measurements can detect atmospheric precipitation with different water vapor channels, but they are limited by vertical resolution and the cloud area coverage. The PRO observations offer a possibility for evaluating the performance of various cloud microphysics schemes. The motivation of this study is to assess *whether the PRO observation can be used to evaluate the performance of model cloud microphysical parameterizations on Typhoon cases.*

70   The study focuses on three typhoon cases, including two in 2019 and one in 2021. The first one is Typhoon Bualoi, which formed on 19 October 2019, and under a favorable condition of low vertical wind shear and warm sea surface temperature, it rapidly intensified to become a typhoon on the next day. Two days later, it intensified rapidly into a Category-5 typhoon. Despite Bualoi not making landfall in Japan, the heavy rainfall caused floods and landslides, which resulted in casualties and substantial property damage. The second case is Typhoon Matmo, which formed on 28 October 2019 over the South China

75   Sea and then weakened after making landfall in central Vietnam on 30 October. It brought strong winds and heavy rainfall, causing flooding and road closures. Typhoon Matmo destroyed ~2,700 houses, causing more than 165 million USD in damage in Vietnam. The third case is Typhoon Kompasu in 2021, which formed through the merging of two tropical depressions embedded within a monsoonal circulation. The typhoon affected many areas, including the Philippines, Taiwan, southeast China, and Vietnam. It caused significant damage to the Philippines, and consequently, the name "Kompasu" was removed

80   from the naming list of tropical cyclones. These three typhoon cases were selected because one PRO profile was located very close to the vertex center for each case during the maturity stage of the typhoons. The relative locations can be found in Fig. 1 and Table 1.

Table 1. A list of observations near each typhoon case, including GNSS RO from FORMOSAT-7/COSMIC-2, PRO from PAZ, and radiosonde (RAOB).

Typhoon	Simulation Period	PAZ PRO, FS7/C2 RO, RAOB	location
BUALOI	2019/10/23 06 UTC ~ 2019/10/24 00 UTC	PAZ1.2019.296.21.41.G14	26.340ºN, 141.570ºE
		wetPf2_C2E1.2019.296.21.25.R17	23.215ºN, 137.081ºE
MATMO	2019/10/29 18 UTC ~ 2019/10/30 12 UTC	PAZ1.2019.303.09.35.G16	14.370ºN, 109.300ºE
		wetPf2_C2E2.2019.303.07.09.G05	13.070ºN, 106.917ºE
		wetPf2_C2E2.2019.303.07.22.G27	16.720ºN, 106.822ºE
		wetPf2_C2E2.2019.303.09.07.R21	16.549ºN, 105.140ºE
		wetPf2_C2E3.2019.303.09.33.G15	9.495ºN, 113.326ºE
		wetPf2_C2E4.2019.303.07.39.G27	12.254ºN, 105.236ºE
		wetPf2_C2E4.2019.303.09.13.G15	15.483ºN, 111.470ºE
		wetPf2_C2E4.2019.303.11.09.R07	13.757ºN, 109.022ºE
		wetPf2_C2E4.2019.303.11.10.G03	10.255ºN, 107.977ºE
		wetPf2_C2E5.2019.303.10.17.G22	13.532ºN, 111.725ºE
KOMPASU	2021/10/12 06 UTC ~ 2021/10/13 00 UTC	PAZ1.2021.285.23.27.G04	18.840ºN, 112.650ºE
		wetPf2_C2E2.2021.285.21.37.G24	22.326ºN, 114.932ºE
		wetPf2_C2E5.2021.285.22.03.G03	15.476ºN, 111.449ºE
		wetPf2_C2E5.2021.285.22.06.R02	21.835ºN, 117.528ºE
		wetPf2_C2E5.2021.285.22.12.G24	15.776ºN, 111.701ºE
		sonPrf_C2E2.2021.285.21.37.G24	22.320ºN, 114.170ºE
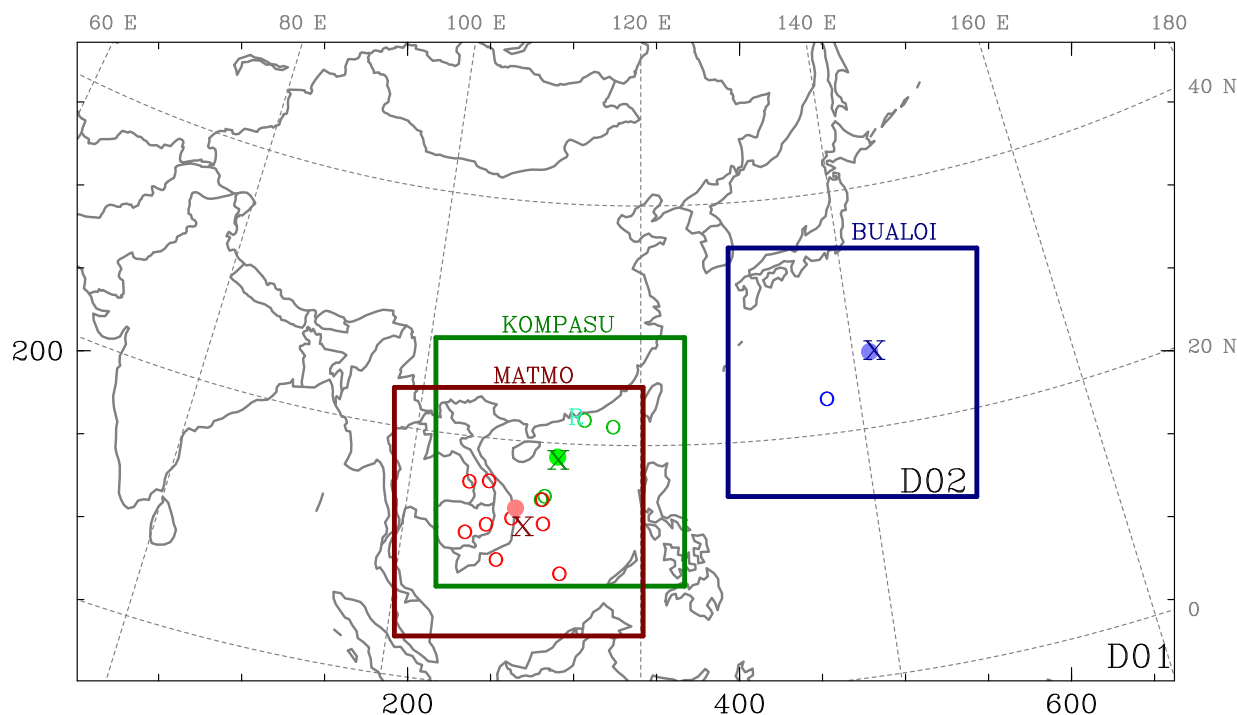
Figure 1. The domain coverage with the same Domain 1 (D01) and varied Domain 2 (D02) for individual cases, as indicated by colored squares. The symbols represent different data sources: solid dots for PRO data from PAZ, hollow circles for GNSS RO data, the character 'R' for radiosonde, and cross signs for typhoon locations from JTWC.

In this study, we perform high-resolution WRF model simulations for the three typhoon cases and compare the simulated differential polarimetric phase shifts with the PAZ PRO observations. The WRF model configuration and the experimental design are described in Sect. 2, and the PRO forward operator is introduced in the same section. Sect. 3 presents the simulated results with different initial conditions and microphysical parameterizations. Verification against the PRO observations for the three typhoon cases are presented in Sect. 4, and the analysis of the uncertainties, including model initial conditions, difference between model and observed storm location, as well as details of the simulated cloud distributions, etc., are discussed in the same section. Finally, the conclusion will be presented in Sect. 5.

2 WRF model and the PRO forward operator

2.1 Model configuration and experimental designs

The Advanced Research version of WRF (WRF-ARW, hereinafter the WRF Model; Skamarock et al., 2021) is a fully compressible, nonhydrostatic model widely used by the research community and operational centers. In this study, the WRF model version 4.2 is used with two model domains at resolutions of 15 km and 3 km, respectively (Fig. 1). The outermost domain (D01) is fixed for all three typhoon cases with 662×386 grid cells, and the inner domain (D02), with 751×751 grid

cells, is placed near the center of the storm for each individual typhoon case. The domain coverages for each typhoon case are depicted in Fig. 1. The model consists of 52 layers with the model top at 20 hPa. The initial time for the WRF simulation varies according to each typhoon case, but the total forecast length is a consistent window of 18 hours. The initial times are 0600 UTC 23 October 2019 for Typhoon Bualoi, 1800 UTC 29 October 2019 for Typhoon Matmo, and 0600 UTC 12 October 2021 for Typhoon Kompasu (Table 1).

The accuracy of model simulations is impacted by uncertainties associated with initial conditions and model formulation such as physical parameterization (Ehrendorfer, 1997). To evaluate the uncertainties, we conduct WRF simulations with two sets of initial conditions and five microphysics parameterization schemes. Two global analyses, including NCEP FNL (Final) analysis and ERA5 reanalysis, were adopted for the WRF initial conditions, while NCEP FNL at 6-h interval and ERA5 at 1-h interval were used for the boundary conditions. For both initial conditions, the same horizontal resolution of 0.25º by 0.25º is adopted. Since the focus of this study is cloud microphysical parameterization, we keep all other physical parameterizations the same for all experiments, with the exception of microphysics. These common physical parameterizations include: Kain–Fritsch cumulus parameterization (Kain, 2004), Yonsei University (YSU) planetary boundary layer (PBL) parameterization scheme (Hong et al., 2006), and a new version of the Rapid Radiative Transfer Model (RRTMG) for the radiation effects (Iacono et al., 2008). Notice that the cumulus convective parameterization scheme was applied only for the 15-km domain.

It should be noted that only relative humidity from either ERA5 or NCEP FNL is ingested in the WRF preprocessing system (WPS) for the model initialization. None of the hydrometeor information from the global analyses was used in the WRF initial condition. The precipitation structure (i.e., hydrometeor distribution) in the model has to be developed through model integration with the microphysics parameterization. There are many options of microphysics schemes available in the WRF model, and each parameterization has its own unique way of handling microphysical processes. In this study, we evaluate the performance of the microphysics parameterization with five microphysics schemes, such as Purdue Lin scheme (Chen & Sun, 2002), WSM6 6-class graupel scheme (Hong and Lim 2006), Goddard 4-ice scheme (Tao et al., 1989, 2016), Thompson graupel scheme (Thompson et al., 2008), and Morrison 2-moment scheme (Morrison et al., 2009). Table 2 lists the abbreviated names and corresponding WRF options for these microphysics schemes used in the study. These schemes have been used in operations and research by the Numerical Weather Prediction (NWP) community.

Table 2. The abbreviated names and microphysics schemes used in the study and their corresponding WRF options.

Abbreviated name	Microphysics	WRF options
PurdueLin	Purdue Lin scheme	2
WSM6	WRF Single-Moment 6-class scheme	6
Goddard	Goddard 4-ice microphysics scheme	7
Thompson	New Thompson et al. scheme	8
Morrison	Morrison double-moment scheme	10

The microphysics parameterization schemes model the microphysical processes and the evolution of different hydrometeor species, such as water vapor, cloud water, rain water, ice, snow, graupel, hail, etc. Within these five schemes, Thompson and Morrison schemes both are a double moment scheme, which consider the number concentration and cloud

condensation nuclei effects. The Purdue Lin, WSM6, and Goddard schemes are single moment schemes, and all with ice, snow, and graupel processes. The difference between Goddard scheme and the other two is that it predicts hail and graupel separately, which provides effective radii for radiation. More detail for the microphysics schemes in the WRF model can be found in Skamarock et al. (2021).

135 WRF simulations initialized with the ERA5 and NCEP FNL and the five microphysics schemes are run for 18 h for the three typhoon cases. Thus, there are a total of 30 WRF simulations. We identify each run by a string composed of the initial data source, the typhoon case name, and the microphysics scheme. For example, the simulation initialized from ERA5 and used the Purdue Lin scheme for typhoon Bualoi is named ERA5_Bualoi_PurdueLin.

2.2 PRO forward model

140 The variable from polarimetric RO is the differential phase shift (ΔØ) between the horizontal wave (Ø$_h$) and vertical wave (Ø$_v$), which is the additional excess of the phase delay due to precipitation (Cardellach et al., 2015). The polarimetric phase shift in the unit of mm can be represented as

$$\Delta\emptyset = \int_L K_{dp}(l)dl \qquad (1)$$

where K_{dp} is the specific differential phase in mm km^{-1}, and L is the path length of the radio link. Since the K_{dp} is induced by 145 the difference in scattering properties of hydrometeor particles, a simple linear relation between the water content (WC) and K_{dp} is adopted, following the formula presented in Bringi and Chandrasekar (2001) and Padullés et al. (2022), as below.

$$K_{dp}(WC) = \frac{1}{2}C\rho \times WC \times (1 - ar) \qquad (2)$$

where WC indicates the water content of any hydrometeors in ice, snow, rain, etc. in units of $g\ cm^{-3}$, ρ is the particle density in units of $g\ m^{-3}$, and ar is the assumed dimensionless axis ratio of the particle. C is the Rayleigh 150 scattering at the GPS frequency, which is a proportionality constant in 1.6 ($g\ cm^{-3}$)$^{-2}$. For this effort, the variables ρ and ar are set as constants at 0.2 $g\ cm^{-3}$ and 0.5, respectively, following Hotta et al. (2024). While considering the two variables vary for each hydrometeor, we followed the function presented in Fig. 9 of Padullés et al. (2022), which provided a profile for $\rho \times (1 - ar)$ from the freezing level to the cloud top, to calculate the specific differential phase for this study. We create a look-up table based on the profile for the calculation of K_{dp}. The coefficients at heights below the freezing level and above the cloud top are 155 set to the same constant values as those at these two levels.

To calculate the simulated differential phase shift, the WC on each grid point was converted from the three-dimensional hydrometeors into mixing ratio, which included rain, ice, snow, graupel, hail, clouds, etc. Since each PAZ PRO sounding provides latitude, longitude, and height along the 220 ray paths (Padullés et al., 2024), the WRF simulations were interpolated accordingly. Then, the simulated K_{dp} was calculated by Equation (2) at the same location and height as PAZ PRO, 160 and the integral of K_{dp} along the raypath through the Equation (1) for the ΔØ can be derived. A time interpolation by selecting two model outputs closest to the PRO observation time was conducted as well for the comparisons.

3 Simulated results

The model initializations from these two data sources, NCEP FNL and ERA5, already showed significant differences before the numerical model integration. Using Typhoon Bualoi as an example the initial intensity (i.e. sea level pressure, SLP)

165 and total precipitable water (TPW) from NCEP FNL (Fig. 2b) is more intense than that from ERA5 (Fig. 2a). The difference in intensities between the two analyses can be more than 30 hPa. Besides, the TPW distribution initialized with NCEP is about 80 mm near the inner core and exhibits more symmetry than that of ERA5. This discrepancy illustrates that the model initialization from different global analyses already possesses the uncertainties from the beginning.
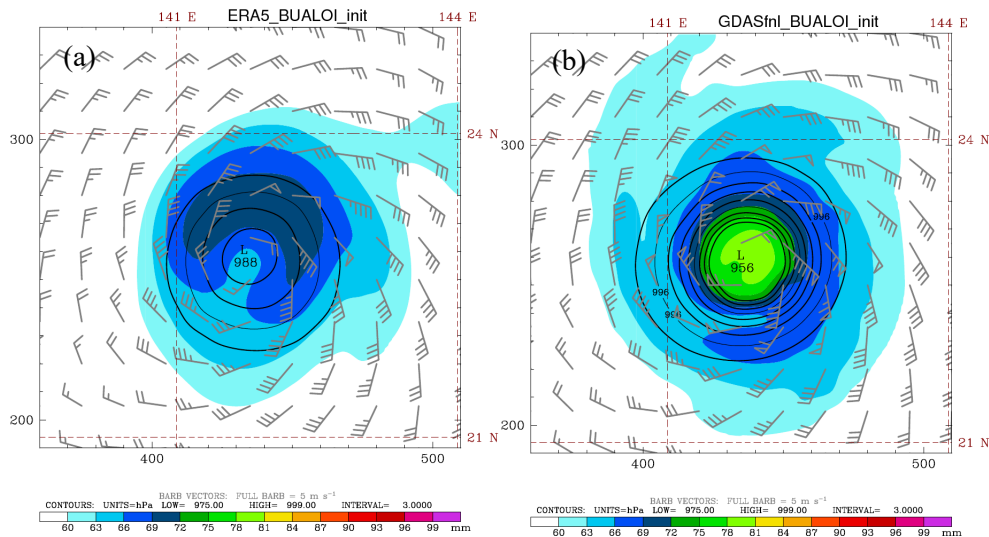
170 **Figure 2. Total precipitable water in color (mm), sea level pressure in contour (hPa), and wind vectors (m s⁻¹) for the WRF initial conditions from (a) ERA5 and (b) GDAS Fnl for the Bualoi case.**

Besides the initial sources, the model parameterizations could also result in variability. Even if the initial condition is identical, using different microphysics parameterization schemes show distinct patterns in precipitation. Fig. 3 displays the SLP and TPW at 18-h forecast from two initial conditions with five microphysics schemes for Bualoi. The simulations show

175 that all the simulated typhoon vortexes have a location error with a westward shift compared to the best track. The maximum location error at the 18-h forecast is about 100 km. After the short-term forecast, the simulated typhoon intensity initialized with ERA5 still exhibited a weaker vortex than that from NCEP. Even though a relatively weaker and drier circulation from the ERA5 initial condition, the TPW in the typhoon circulation is increased to near 100 mm through the WRF integration (Fig. 3a-e). Moreover, the maximum TPW for WRF runs with WSM6 and Morrison microphysics initialized with ERA5 (i.e.,

180 ERA5_Bualoi_WSM6 and ERA5_Bualoi_Morrison, Fig. 3b,e) are larger than that initialized with NCEP FNL (Fig. 3g,j). The horizontal distributions of TPW using the Goddard and Thompson schemes (Fig. 3c,d,h,i) tend to be broader than the other schemes, regardless of the global analysis used to initialize the model. Generally, the simulations show an intense TPW over the western or northwestern part of the vortex, and some differences in scattering precipitation distribution due to typhoon

rotation. Fig. 3 highlights a large variability in the TPW's distributions with different microphysics schemes, which illustrates
185   the uncertainty of the parameterization schemes.
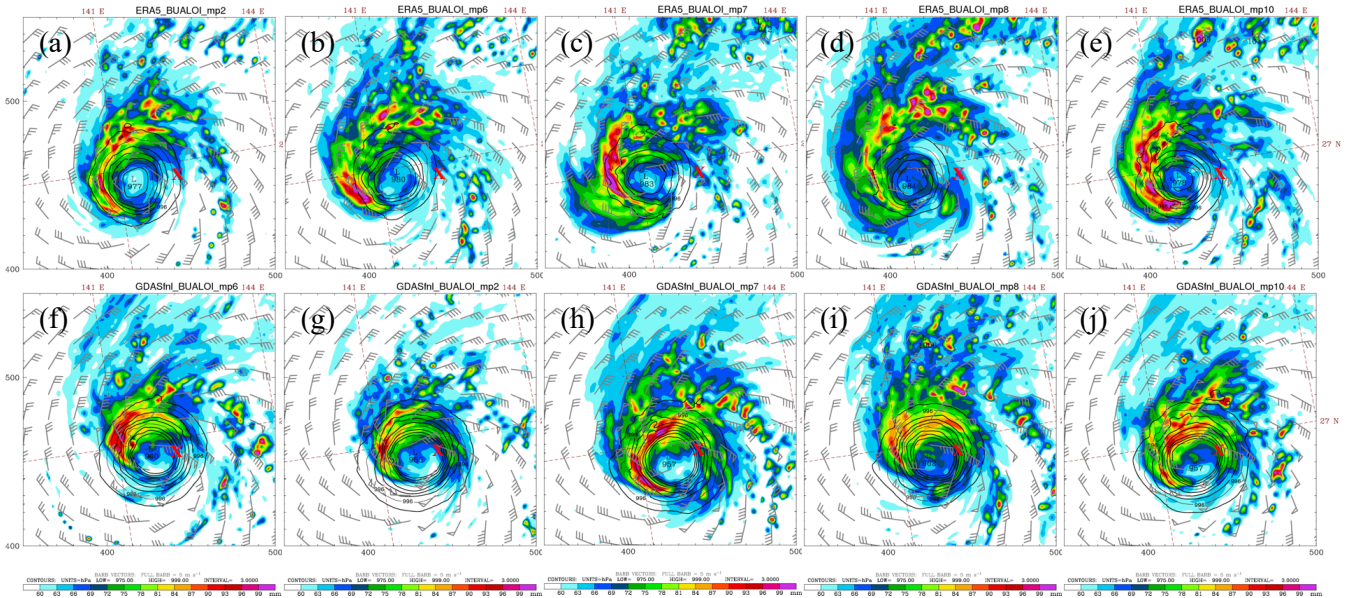
Figure 3. Panels (a)–(e) are similar to Figure 2a for total precipitable water (in color), sea level pressure (in contour), and wind vectors with the initial condition from ERA5, but for WRF 18-hour forecast with different microphysics schemes: (a) Purdue Lin scheme, (b) WSM 6-class graupel scheme, (c) Goddard 4-ice scheme, (d) Thompson graupel scheme, and (e) Morrison 2-moment scheme. Panels (f)-(j) are the same as (a)-(e), but for the initial conditions from GDAS FNL. The red cross sign in each panel, at 26.7ºN and 142.1ºE indicates the observed location of Typhoon Bualoi from the JTWC's best track.

    To evaluate the performance of experiments with different microphysics and initial conditions, verifications against ERA5 reanalysis are conducted on each grid point in the second domain D02. The root mean square errors (RMSE) were computed at each hour of the WRF simulations for each typhoon case. Then, an average is calculated across all the three
195   typhoon cases and the 18-h forecasts, i.e., total of 54 samples for the average, all of which were initialized from ERA5 (Fig. 4). The averaged errors for the five microphysics schemes show comparable patterns in temperature, and only slight deviation presented at 150-600 hPa altitude (Fig. 4a). Regarding the water vapor mixing ratio, it shows more consistent patterns for the five schemes, however, the ERA5_Bualoi_Goddard displays a distinct decreased RMSE at the lower troposphere than the other schemes (Fig. 4b). To make the deviation more apparent, a normalized RMSE is performed (Fig. 4c,d). It is computed
200   by dividing the mean of RMSE at each vertical level. A value equal to one represents mean performance, and a value smaller than one shows better correspondence to ERA5 than the mean. Fig. 4c shows a mixed result, but it is clear to see relatively smaller RMSEs of the Goddard scheme in temperature throughout the troposphere. Regarding the water vapor mixing ratio, it shows an evident outperformance for the ERA5_Bualoi_Goddard than the others at the lower troposphere (Fig. 4d); it has a normalized value of 0.94 at 950 hPa and the others are about 1.02. The verifications for the simulations with the NCEP
205   initialization show a similar conclusion (figure not shown), therefore we will focus on the experiments with the ERA5 initialization for the later discussion.
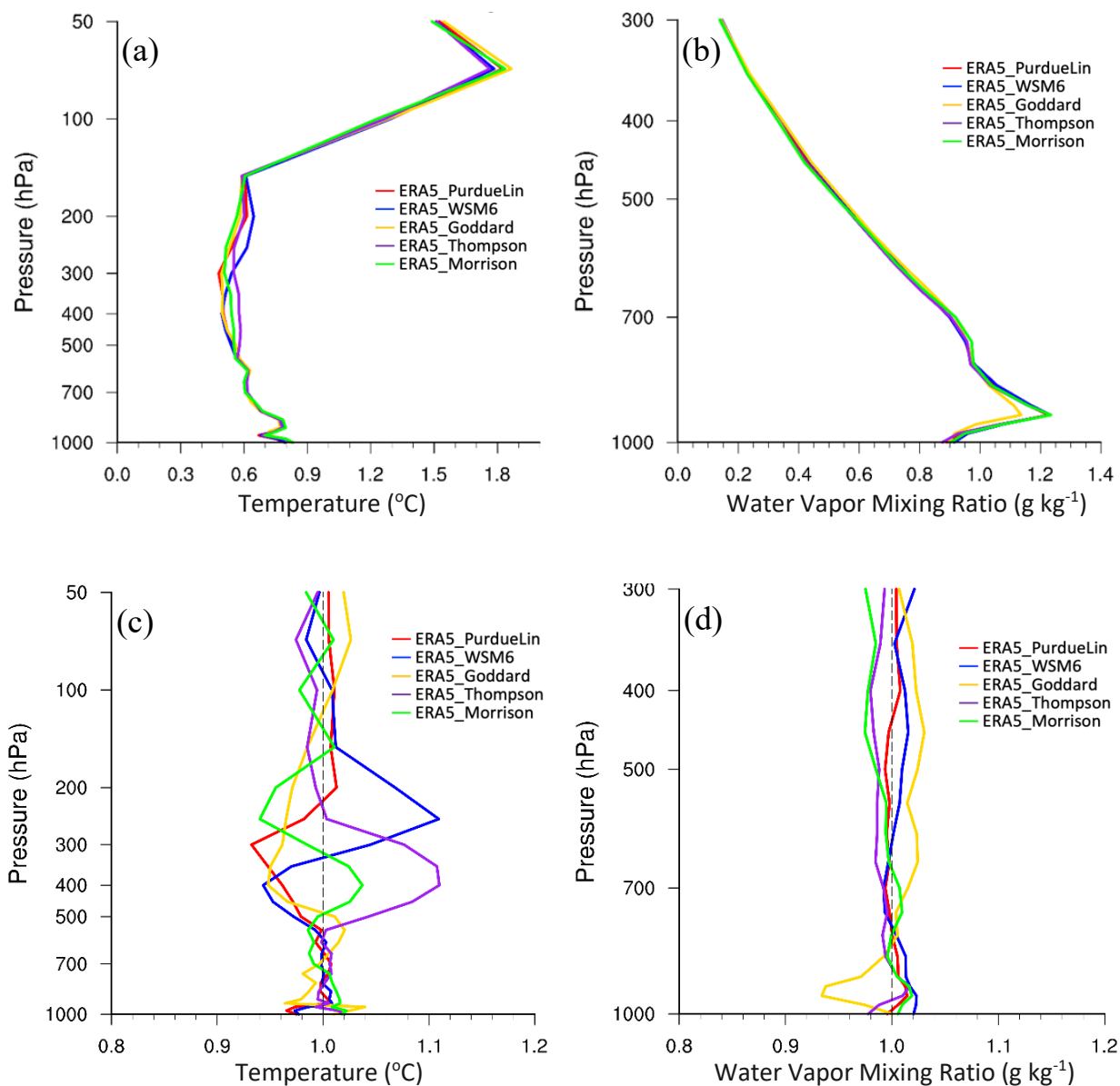
Figure 4. The averaged grid verification for three typhoon cases against ERA5 in RMSE for (a) temperature and (b) water vapor mixing ratio across all simulations during the 18-hour forecasts. Verification was performed at each hour and averaged over all the time and cases, i.e., 18 WRF outputs for each case, thus a total of 54 samples for the average. The red curve represents the PurdueLin scheme, blue represents WSM6, yellow represents Goddard, purple represents Thompson, and green represents the Morrison scheme. (c) and (d) are the same as (a) and (b), respectively, but for the normalized RMSE.

Since traditional GNSS RO data has high accuracy and high vertical resolution, it can be used as verification data. For the three typhoon cases, there are a few soundings close to the typhoon track, including one traditional RO for Typhoon Bualoi, nine ROs for Typhoon Matmo, four ROs and one radiosonde for Typhoon Kompasu. Therefore, a total of 15 observations can

be used for the sounding verification (Table 1). They are indicated in Fig. 1 with the typhoon locations from the Joint Typhoon Warning Center (JTWC) best track. The WRF forecasts, at 1-h intervals, are interpolated to the specific times and locations of 15 soundings for comparison. Similar to Fig. 4, Fig. 5 shows the temperature and water vapor mixing ratio verification. It is evident that the ERA5_Morrison (green curve) has less error in temperature than the other schemes above 10 km (Fig. 5a).

220   However, it is not distinguishable in the water vapor mixing ratio (Fig. 5b). The overall vertical mean error for the five microphysics ranges from -0.34 ~ -0.42 °C in temperature, and -0.16 ~ -0.18 g kg^{-1} in moisture.

In general, the environmental verifications against either ERA5 or the traditional RO and radiosonde do not show significant difference among the five microphysics schemes (Fig. 4,5). WRF simulations with different initial conditions and microphysical parameterizations can produce significant difference in cloud, precipitation structure, and hydrometeors

225   distributions. However, their impact on the large-scale variables is relatively small for an 18-h forecast.
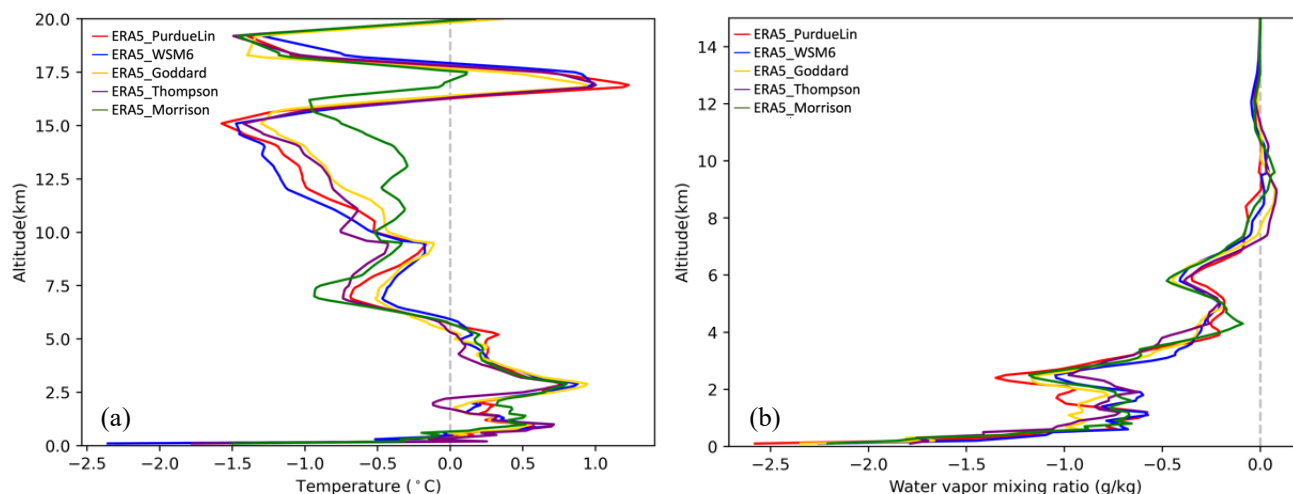
Figure 5. The mean differences for verifications against soundings (15 GNSS RO and 1 radiosonde) in (a) temperature and (b) water vapor mixing ratio across all simulations. The red curve represents the PurdueLin scheme, blue represents WSM6, yellow represents Goddard, purple represents Thompson, and green represents the Morrison
230   **scheme.**

4 Verification against PRO observations

The PRO profile, sensitive to precipitation structure, could be used to evaluate the model hydrometeors' vertical structure in the sum of rain, ice, snow, graupel, hail, etc. We have one PAZ PRO profile available for each typhoon case (Table 1), and each of the PRO sounding is close to the individual typhoon center (Fig. 1); for example, the time and location differences

235   between the PRO location and the storm center are 33 minute and 18.6 km, respectively, for Typhoon Kompasu. In addition, the WRF model has been integrated for more than 15 h before the comparison with of the corresponding PRO data, allowing the model to develop hydrometeors through the cloud microphysical process. To reduce the spatiotemporal error, two model outputs at time close to the PRO observation were linearly interpolated to the observation time of the PRO profile. Even with

the time interpolation, the location of the simulated vortex could differ from the observed location as shown in Fig. 3, and the
240   precipitation distribution would be shifted. To minimize the error due to location difference, the simulated storm center is
relocated to the observed location. The ray trajectory is determined based on the relocated WRF simulations. Then, the
differential phase shift between the PAZ PRO and the WRF simulations can be compared.

4.1 Deterministic run

Fig. 6 shows the WRF simulations with the ERA5 initial conditions and different microphysics for Typhoon Bualoi. The
245   distribution of simulated hydrometeors along the ray path shows the rain species dominates below 5 km and a mixing of frozen
precipitation above this height. Generally, the hydrometeors from the model show large variability. The PurdueLin and WSM6
schemes show a concentration of hydrometeors near the perigee point (26.34ºN, 141.57ºE), and they are both composed of
larger graupel at 5-12 km (Fig. 6a,b). For the Goddard, Thompson, and Morrison microphysics, the snow dominates and has a
larger horizontal extent (Fig. 6c,d,e). Also, some hail is presented around 4-7 km for the Goddard scheme
250   (ERA5_Bualoi_Goddard). The PAZ PRO observation shows a maximum differential phase shift of 35.1 mm at the height of
7.5 km for Typhoon Bualoi. The WRF simulations with various microphysics generally place the peak differential phase at
the altitude close to the PAZ PRO observation, but with a large discrepancy in value. All the simulated ΔØ are smaller than
the observation, except for the ERA5_Bualoi_Goddard. The Goddard schemes and the two-moment schemes (Thompson and
Morrison) show a peak ΔØ at 5-8 km, which is in agreement with the observation (Fig. 6c-e). Among the frozen hydrometeor
255   species, the snow contributed the most, which agrees with the finding in Padullés et al. (2024). The Goddard scheme has the
best performance in terms of differential phase comparison for Typhoon Bualoi. It shows a maximum value of 36.9 mm at
approximately 6.4 km and is comparable with the PAZ PRO in terms of magnitude. Also, it has a very good fit below 5 km,
which is contributed by rain (Fig. 6c). The vertical distribution of the simulated differential phase agrees better with the PRO
data when using the Goddard scheme or the double moment scheme. The best fitting is the experiment using the initial
260   condition from ERA5 and the Goddard scheme.
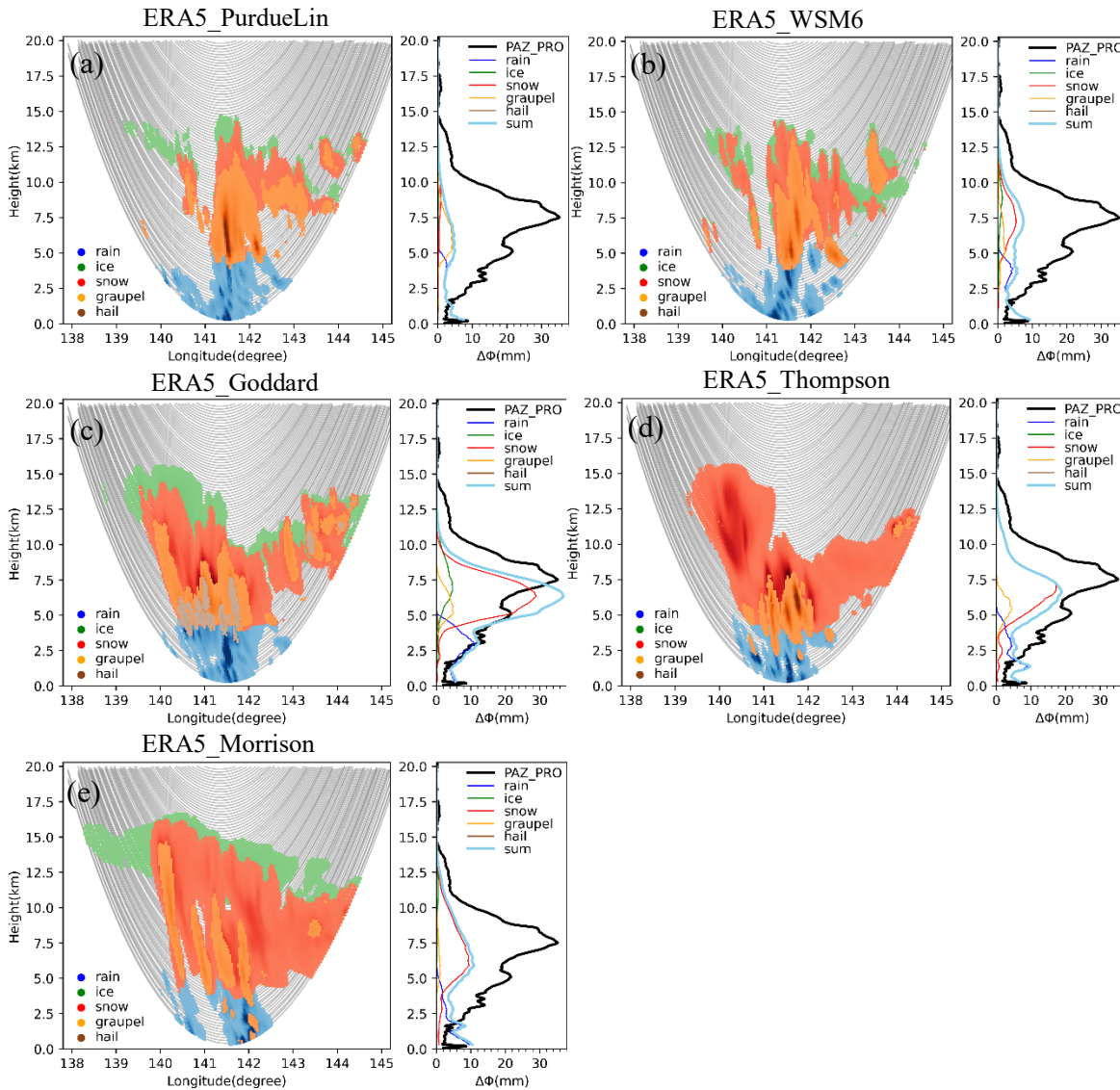
Figure 6. Distribution of simulated hydrometeors along the PAZ raypath (gray curves) on the left panel, and the differential phase shift from PAZ observation (black curve), along with the calculated phase shift for each simulated hydrometeor species on the right panel for the Bualoi simulation with ERA5 as the model initial condition. The 15-h and 16-h WRF simulations are interpolated based on the PRO's time and location. The light blue curve represents the sum of all simulated phase shifts. Panels (a) to (e) represent different microphysics schemes for (a) PurdueLin, (b) WSM6, (c) Goddard, (d) Thompson, and (e) Morrison schemes.

Fig. 7a shows the infrared satellite image of Typhoon Bualoi at 2230 UTC on 23 Oct. 2019, and the observed cloud-top temperature is about -70 degrees. The simulation ERA5_Bualoi_Goddard at 16-h forecast also shows a solid vortex with a low cloud-top temperature of -70 degrees, and the distribution aligns well with the infrared satellite image (Fig. 7). Generally, the extensive cloud coverage of typhoon Bualoi is well captured by ERA5_Bualoi_Gaddard, as well as the small-scale cloud

clusters to the south of the typhoon. The simulations with the other microphysics schemes show large variations, e.g., a small coverage of low cloud-top temperature near the typhoon center for PurdueLin and WSM6, a loose typhoon structure for Thompson, or an overly large typhoon circulation structure with Morrison, that all show significant discrepancies from the

275 observations (figures not shown). Since the ERA5_Bualoi_Goddard is comparable with the PRO observation, this set will be discussed for the other two typhoon cases.
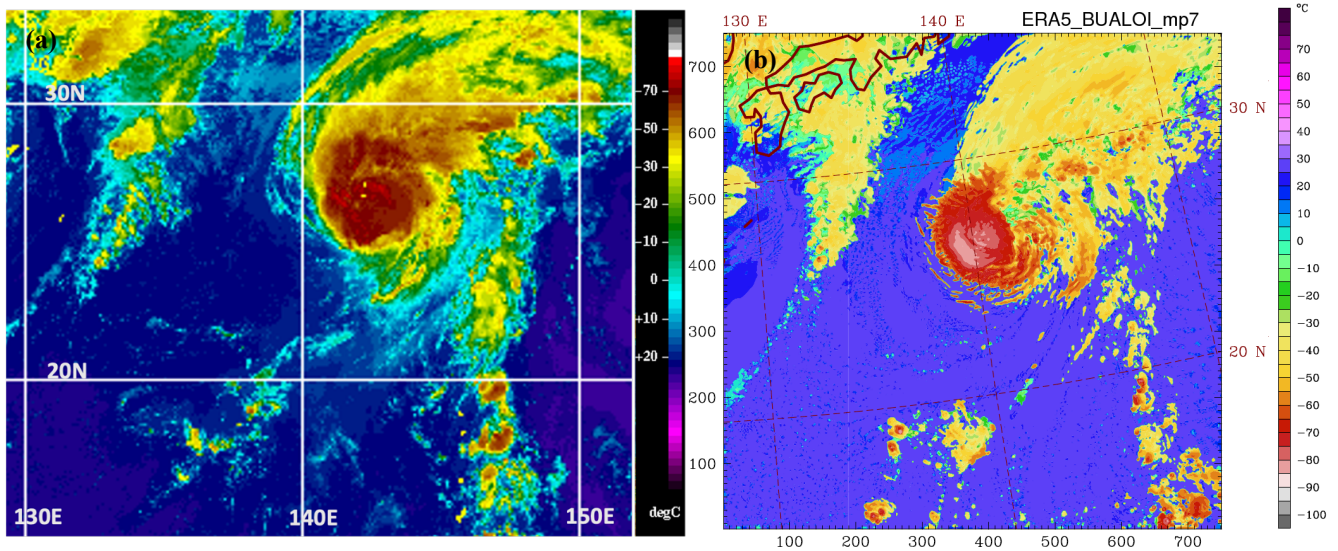
Figure 7. (a) The infrared satellite image with NHC enhancement, adopted from the Cooperative Institute for Meteorological Satellite Studies/University of Wisconsin-Madison (CIMSS), for Typhoon Bualoi at 2230 UTC on 23
280 **Oct. 2019. (b) The 16-h forecast (i.e., 2200 UTC 23 Oct.) cloud top temperature for typhoon Bualoi with the Goddard microphysics and the initial condition from ERA5.**

For Typhoon Matmo (2019), the PAZ PRO observation shows a large $\Delta\text{Ø}$ (more than 20 mm) extending from 3 km to 8 km and has a maximum of 36.7mm at around 5 km (Fig. 8a). The WRF simulation, ERA5_Matmo_Goddard, also shows a large $\Delta\text{Ø}$ below 8 km, which is primarily contributed by snow in the mid-troposphere and by rain in the lower troposphere. In
285 general, the simulated $\Delta\text{Ø}$ shows comparable values and vertical variation with the PRO measurement, although an overestimation is found below 4 km. The vertical distribution of $\Delta\text{Ø}$ is consistent between the model simulation and the PRO observation between 4 to 10 km, which is very encouraging. The simulated hydrometeors show that the graupel and hail occur in the eastern part of the ray, and snow can be found along the ray path extending from 2.5 km to 12.5 km, with ice at higher altitudes. For Typhoon Kompasu, the PRO shows a $\Delta\text{Ø}$ of 20 mm at a higher altitude (8 km) and decreases below the height
290 until 5 km, and then increases again toward the surface (Fig. 8b). The simulated $\Delta\text{Ø}$ does not reproduce such variation. The WRF simulation shows an increased $\Delta\text{Ø}_{sum}$ with decreasing altitude, and without a peak near 8 km like the observation. Notice that the verifications against ERA5 for ERA5_Kompasu_Goddard show larger RMSEs than the other two cases in both temperature and moisture at the mid- and low troposphere (figure not shown). It indicates that the overall simulation of Typhoon Kompasu by the WRF model is not as successful as the other two cases. Nevertheless, the simulated maximum $\Delta\text{Ø}$

295   is about 24 mm at 2.5 km, which agrees with the observation in terms the magnitude but at a higher altitude. The large

simulated ΔØ is contributed by the snow species. Additionally, most hydrometeors are distributed closer to the western part of

the rays.
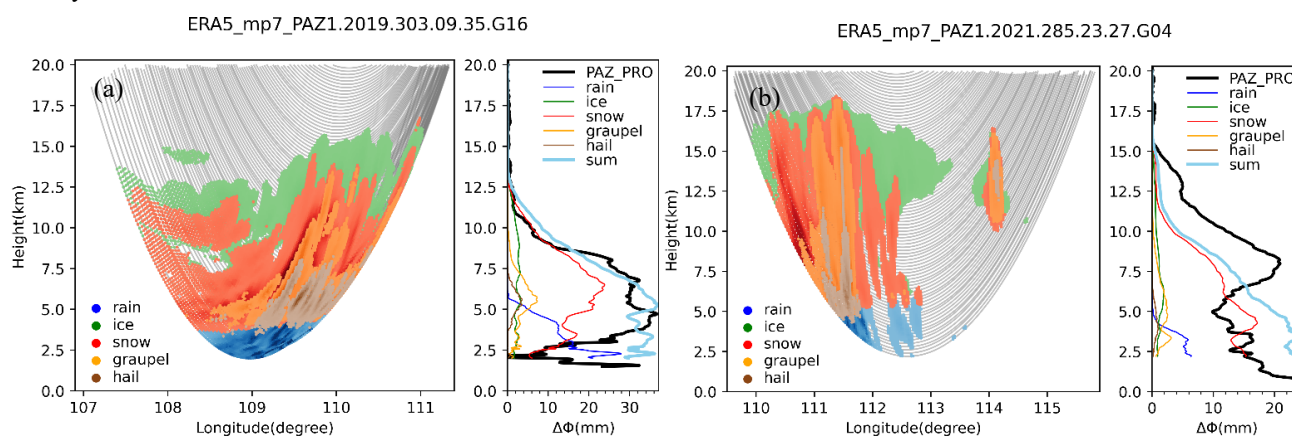
Figure 8. Distribution of simulated hydrometeors along the PAZ raypath on the left panel, and the differential phase
300   **shift from PAZ observation (black curve), along with the calculated phase shift for each simulated hydrometeor species**
on the right panel. The light blue curve represents the sum of all simulated phase shifts. Panels (a) and (b) show
simulations using the Goddard microphysics scheme for Typhoon Matmo and Typhoon Kompasu, respectively.

To investigate why the ΔØ simulations for Typhoon Kompasu do not align well with the PRO, synoptic-scale verifications

are conducted using a similar method illustrated in Fig. 4a,b, for three typhoon cases, which are initialized with ERA5 and

305   simulated using the Goddard microphysics scheme (i.e., ERA5_Bualoi_Goddard, ERA5_Matmo_Goddard, and

ERA5_Kompasu_Goddard). Fig. 9 presents the verifications in temperature and water vapor mixing ratios for the three

simulations. Below 300 hPa, ERA5_Kompasu_Goddard generally exhibits a larger RMSE than the other two cases,

particularly for moisture (Fig. 9b), indicating a greater discrepancy of the simulated synoptic environment of

ERA5_Kompasu_Goddard from the ERA5 analysis. Discrepancies in the simulated larger-scale environment could lead to

310   deviations in the simulated mesoscale typhoon circulation and associated precipitation, thereby preventing it from capturing

the observed ΔØ variations.
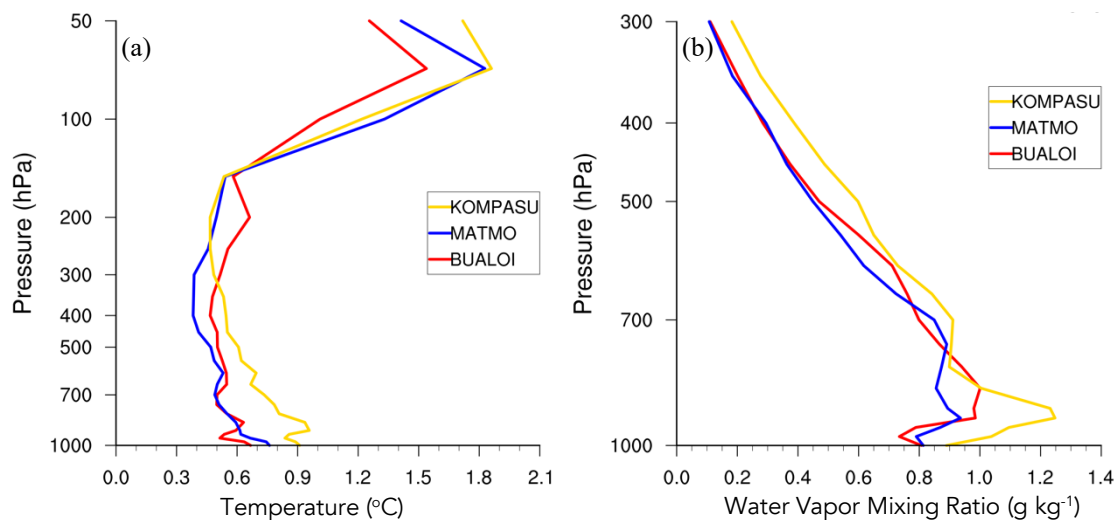
Figure 9. Averaged grid verification against ERA5 in RMSE for simulation with the Goddard microphysics scheme for (a) temperature and (b) water vapor mixing ratio across all simulations during the 18-hour forecasts. The red curve corresponds to ERA5_Bualoi_Goddard, the blue curve to ERA5_Matmo_Goddard, and yellow curve to ERA5_Kompasu_Goddard.

4.2 Ensemble run with Goddard microphysics

Evaluating hydrometeors within the typhoon circulations can be a challenge because the convective systems surrounding the tropical cyclone is highly variable in time and space. It is difficult to obtain a perfect simulation of an observed convective system surrounding the eye wall at the right time and location. To gain insight on the uncertainties of simulated convective systems, we perform ensemble forecasts for the three typhoon cases. The ERA5_Bualoi_Goddard experiment is adapted as an example. The same initial condition from ERA5 for the deterministic run in Sect. 4.1 was used to create perturbations for 36 ensemble members by using the RANDOMCV function in WRFDA, which made perturbations in control variable space (Barker et al. 2012). Fig. 10 illustrates the variance and ensemble mean for the 36 ensemble initializations at the initial time for Typhoon Bualoi. It shows significant variations in precipitable water over the region (20°N-30°N, 135°E-150°E), indicating large model uncertainties over this area, in the vicinity of the PAZ PRO profile. The same process as the deterministic run, the 36 ensemble members were conducted for 18 h forecasts, and then the PRO data can be used to evaluate ensemble uncertainty.
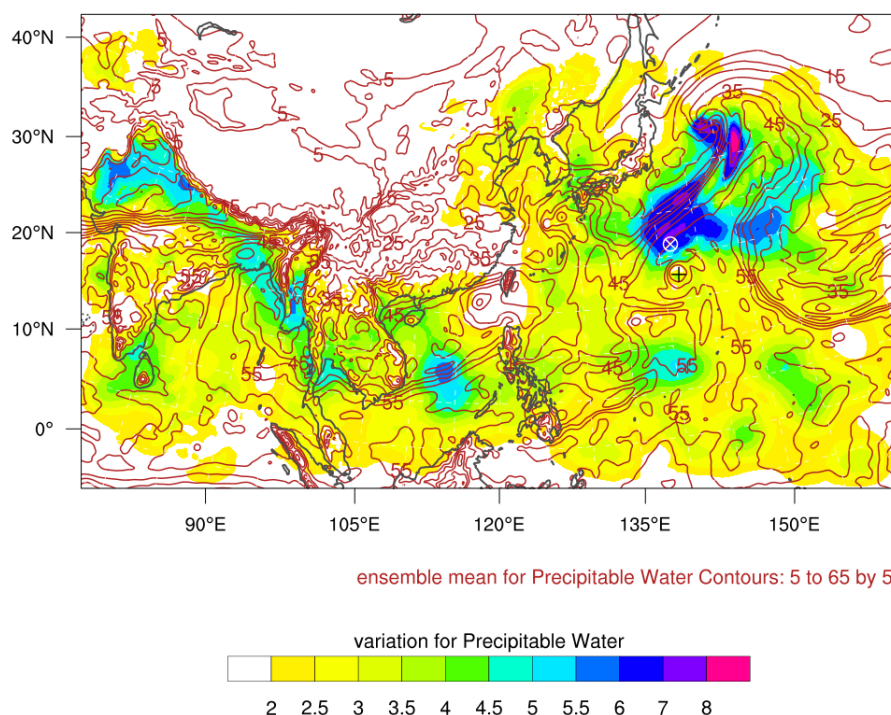
Figure 10. The variance (shaded) and ensemble mean (contour) of the precipitable water for the 36 ensemble members.
330 **The cross sign indicates the location of the PRO observation, and the plus sign indicates the best track for Typhoon Bualoi.**

After integrating each of the 36 ensemble members for 15 hours and 40 minutes, the simulation time was closest to the observation time of PRO (i.e., 2019-10-23 21:41:19). The PRO ray path shows a northeast-southwest orientation and passes through the typhoon center (Fig. 11). Fig. 11 shows the radar reflectivity simulation for each member. There are significant variations among the members. Some members, such as member 13, exhibit asymmetric and incomplete eyewall. In addition to slight differences in the typhoon's position, the typhoon intensity and circulation distribution also display significant variations across members. Therefore, a single numerical model simulation may not be representative for the comparison with PRO observations. To capture the uncertainties, we performed an ensemble mean of the 36 simulations and then compared it with the PRO observations.

340
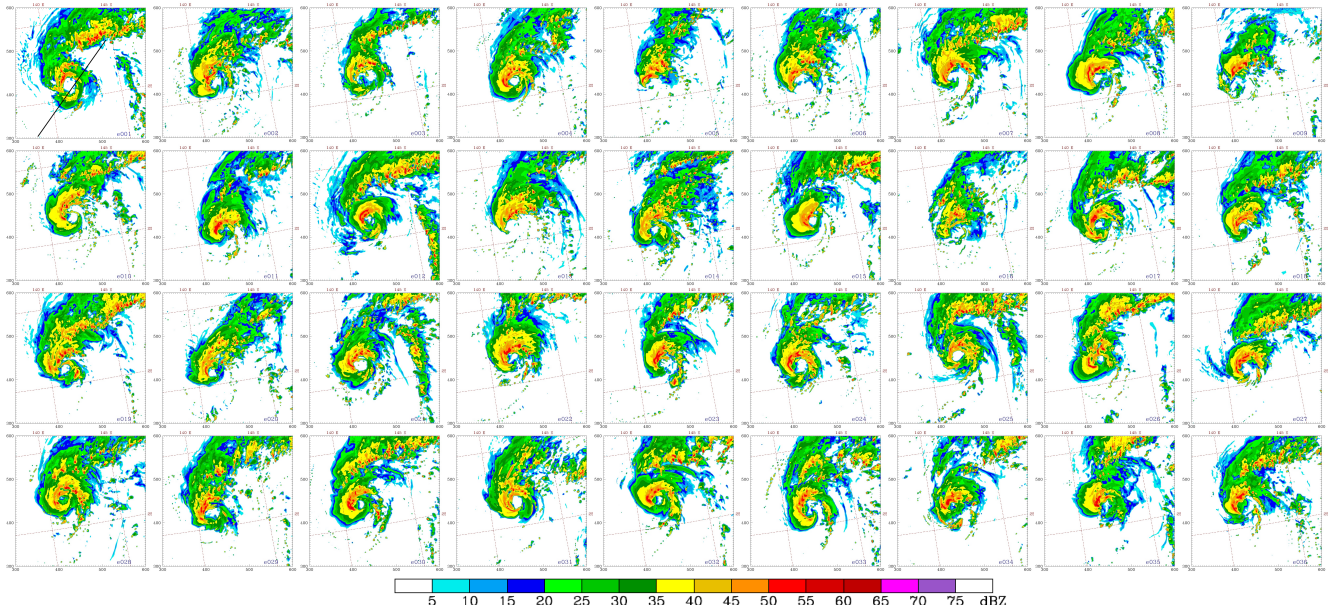
Figure 11. Maximum simulated equivalent radar reflectivity factor for each ensemble member at the 15-hour and 40-minute forecast, compared to the PAZ observation (2019-10-23 21:41:19) for the Bualoi case. The black line in the upper-left panel indicates the PAZ ray path, and the panels, arranged from left to right and top to bottom, follow the member order from 1 to 36.

Because of the difference between the simulated and observed typhoon positions, we considered the vortex position error in each member and adjusted location of the calculated ray path accordingly. After averaging the calculated $\Delta\varnothing$ from all members, the ensemble mean for the three typhoon cases are shown in Fig. 12. For the Bualoi case, Fig. 12a displays that the ensemble-averaged hydrometeor distribution is more homogenous, and the extreme values are smoothed out, the maximum total $\Delta\varnothing$ of the ensemble mean is 28.8 mm (Fig. 12a), unlike the more distinct patterns in the single experiment with a maximum of 36.9 mm (Fig. 6c). Despite this, the pattern of $\Delta\varnothing_{sum}$ remains consistent with the PRO observations. Fig. 12b shows the variations in the simulated $\Delta\varnothing_{sum}$ across the 36 members and the ensemble mean for Typhoon Matmo. Within one standard deviation, the ensemble mean can encompass the entire PRO observed profile, showing that the ensemble mean is a good representation of the ensemble. For Typhoon Matmo, the overall result of the ensemble mean is similar to that of the single deterministic forecast (Fig. 12c and 8a), with a maximum $\Delta\varnothing$ of 43 mm, which is approximately 6 mm larger than the single simulation. The ensemble mean exhibits a smoother vertical variation in the total differential phase shift, but the overall pattern still closely resembles the PRO observations (Figure 12c,d). In contrast, for Typhoon Kompasu, even with 36 ensemble simulations, the simulated phase variations still exhibit significant differences compared to PRO observations. The maximum $\Delta\varnothing_{sum}$ occurs at 5.5 km with a value of 28.1 mm for the ensemble mean, while it is around 21 mm at 8 km from PRO (Fig. 12e). The ensemble results indicate that the simulated phase shift is underestimated above 7.5 km and overestimated below this level for the Kompasu case (Fig. 12f). This could be related to the performance of the synoptic-scale simulation for Typhoon Kompasu since the background field for the perturbations came from the same source as in the deterministic run.

Generally, the variation of the differential polarimetric phase shift from PAZ PRO is within one standard deviation of the ensemble mean for ERA5_Bualoi_Goddard and ERA5_Matmo_Goddard, which indicates good simulations of the hydrometeors from the numerical model. Consequently, the usefulness of the PRO data for the evaluation of cloud microphysical parameterization is evident.
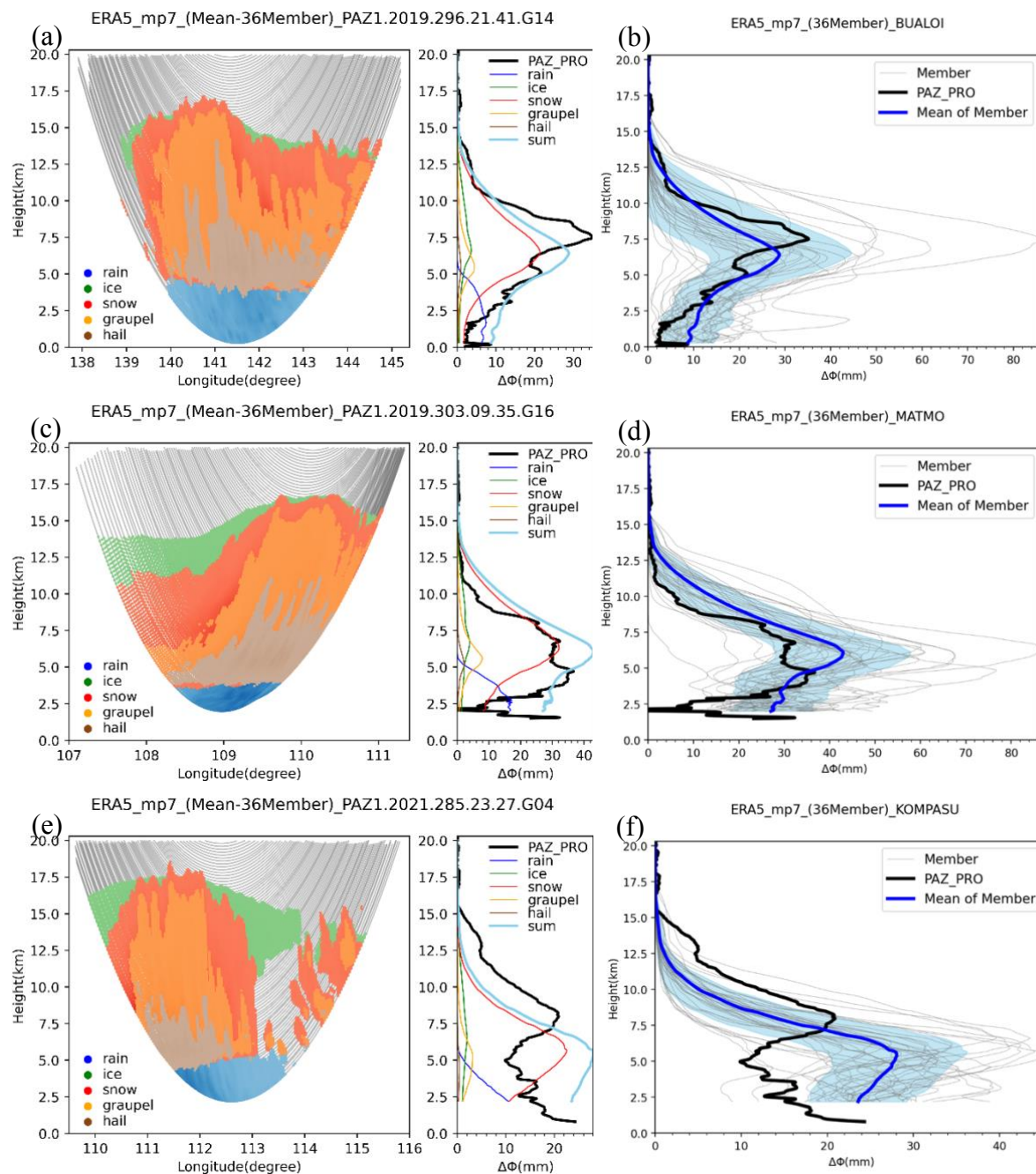
Figure 12. (a) Same as Figure 7a, but for the ensemble mean and (b) the total differential phase shift for each ensemble member for Typhoon Bualoi. The light blue shadow described the range for one standard deviation. Panels (c),(d) and (e),(f) are the same as (a),(b), but for Typhoon Matmo and Typhoon Kompasu, respectively.

370

5 Conclusions

The prediction of cloud and precipitation by numerical models is handled by microphysical parameterization schemes, which are commonly developed based on laboratory experiments and empirical data. The evaluation of these microphysical parameterization schemes has been a challenge, because of the lack of observations. By tracking the differential phase shift

375 between horizontal and vertical polarization of GNSS signals as they transverse through precipitation systems, the polarimetric radio occultation (PRO) technique provides information on cloud hydrometeors. Such measurements can potentially be used to evaluate the performance of cloud microphysical parameterization schemes of numerical models.

In this study, we conduct WRF model simulations for three typhoon cases from 2019 and 2021. For each typhoon case, the simulations were conducted with two initial conditions (i.e., ERA5 and NCEP FNL) and five microphysics schemes

380 (PurdueLin, WSM6, Goddard, Thompson, and Morrison). The results show significant variability in the distribution of the simulated hydrometeors, depending on initial conditions, microphysics parameterizations, typhoon locations, and the perturbations in the ensemble forecasts, etc. The WRF simulations are interpolated to the location of PAZ PRO observations, taking into consideration of position error of the model tropical cyclones. The simulated cloud hydrometeors are then used to produce the simulated PRO profiles using a forward operator for comparison with the PAZ PRO observations.

385 The WRF simulation initialized with the ERA5 reanalysis and using the Goddard microphysics scheme performed best both in terms of large-scale verification against the global analyses as well as the differential phase verification against the PAZ PRO data. The superior performance of the Goddard microphysics scheme was supported by both a deterministic forecast as well as the ensemble mean for Typhoon Bualoi and Typhoon Matmo. Furthermore, the PRO observations fell within the one standard deviation range of the ensemble members for both cases, demonstrating the robustness of the verification.

390 Considerable discrepancy between simulated and observed PRO was found for the third case, i.e., Typhoon Kompasu. The verification against ERA5 reanalysis showed that the WRF simulation of Typhoon Kompasu had the largest errors among the three cases.

Even though these preliminary results are encouraging, the limitations of this study should be noted. First, only three PRO profiles for the three typhoon cases were examined. More PRO observations for additional tropical cyclone cases should be

395 evaluated to establish the statistical robustness of the conclusions. Moreover, the simulated convective precipitation systems are transient and highly variable, and can vary significantly due to uncertainties in vortex location, large-scale circulations, detailed cloud microphysics, and the model's representativeness of other physical processes (i.e., boundary layer, radiative forcing, … etc.). It would be desirable to improve the accuracy of the large-scale and mesoscale simulation of the tropical cyclones prior to the evaluation of the simulated cloud hydrometeors.

400   With the availability of more PRO data from commercial sources, we plan to expand our study for more typhoon cases in the future. In addition, we will evaluate the performance of cloud microphysics schemes against PRO observation under different weather regimes (e.g., atmospheric river, Mei-Yu front, mesoscale convective systems, etc.).

Data and code availability

The initial conditions for all the simulations are downloaded from https://cds.climate.copernicus.eu/api/v2 for ERA5 and
405   https://rda.ucar.edu/datasets/d083003/ for NCEP Fnl. The GNSS RO profiles for the validation are downloaded from https://tacc.cwa.gov.tw/data-service/fs7rt_tdpc/level2/wetPf2/. The WRF model is an open-source model, and it can be found at https://github.com/wrf-model/WRF.

Author contributions

Conceptualization, SYC and YHK; Data Curation and Methodology, SYC, HWL, and RP; Validation, SYC and HWL; Formal
410   Analysis, SYC, YHK, RP, EC, and FJT; Writing - Original Manuscript, SYC; Writing - Review and Editing, SYC, YHK, EC, FJT, and RP.

Competing interests

The authors have no competing interests.

Acknowledgments

415   This research was supported jointly by Taiwan National Science and Technology Council (NSTC) under Grant NSTC 112-2119-M-008-012 and NSTC 113-2111-M-008-019, and Taiwan Space Agency (TASA) under Grant TASA-S-1130319. The National Center for High-performance Computing (NCHC) is acknowledged for providing computational and storage resources. The efforts of FJT were performed at the Jet Propulsion Laboratory, California Institute of Technology, under a contract with NASA.

References

420   Anthes, R. A.: Exploring Earth's atmosphere with radio occultation: Contributions to weather, climate and space weather, Atoms. Meas. Tech., 4, 1077-1103, doi:/10.5194/atm-4-1077-2011, 2011.

Barker, D., Huang, X.-Y., Liu, Z., Auligné, T., Zhang, X., Rugg, S., et al.: The weather research and forecasting model's community variational/ensemble data assimilation system: WRFDA. Bull. Amer. Meteor. Soc., 93, 831-843, doi:10.1175/BAMS-D-11-00167.1, 2012.

Bringi, V. N. and Chandrasekar, V.: Polarimetric Doppler weather radar: principles and applications, Cambridge University Press, doi:10.1017/CBO9780511541094, 2001.

Cardellach, E., Tomás, S., Oliveras, S., Padullés, R., Rius, A. and de la Torre-Juárez, M., et al: Sensitivity of PAZ LEO polarimetric GNSS radio-occultation experiment to precipitation events. IEEE Trans. Geosci. Remote. Sens., 53, 190-206. doi:10.1109/TGRS.2014.2320309, 2015.

Cardellach, E., Padullés, R., Tomás, S., Turk, F. J., Ao, C. O., and de la Torre-Juárez, M.: Probability of intense precipitation from polarimetric GNSS radio occultation observations. Quart. J. Roy. Meteor. Soc., 144, 206-220, doi:/10.1002/qj.3161, 2018.

Cardellach, E., Oliveras, S., Rius, A., Tomás, S., Ao, C. O., Franklin, G. W., et al.: Sensing heavy precipitation with GNSS polarimetric radio occultations. Geophys. Res. Lett., 46, 1024-1031, doi:/10.1029/2018GL080412, 2019.

Chang, C. C. and Yang, S. C.: Impact of assimilating Formosat-7/COSMIC-II GNSS radio occultation data on heavy rainfall prediction in Taiwan. Terr. Atmos. Ocean. Sci., 33, 7, doi:/10.1007/s44195-022-00004-4, 2022.

Chen, S. H. and Sun, W. Y.: A one-dimensional time dependent cloud model. J. Meteorol. Soc. Japan. Ser. II., 80, 99-118, doi:/10.2151/jmsj.80.99, 2002.

Chen, S. Y., Kuo, Y. H., and Huang, C. Y.: The impact of GPS RO data on the prediction of tropical cyclogenesis using a nonlocal observation operator: An initial assessment. Mon. Wea. Rev., 148, 2701-2717, doi:/10.1175/MWR-D-19-0286.1, 2020.

Chen, S. Y., Shih, C. P., Huang, C. Y., and Teng, W. H.: An impact study of GNSS RO data on the prediction of Typhoon Nepartak (2016) using a multiresolution global model with 3D-hybrid data assimilation. Wea. Forecasting, 36, 957-977, doi:/10.1175/WAF-D-20-0175.1, 2021.

Cucurull, L.: Recent impact of COSMIC-2 with improved radio occultation data assimilation algorithms. Wea. Forecasting, 38, 1829-1847, doi:/10.1175/WAF-D-22-0186.1, 2023

Ehrendorfer, M.: Predicting the uncertainty of numerical weather forecasts: A review. Meteor. Z., 6, 147-183, doi:/10.1127/metz/6/1997/147, 1997.

Gleisner, H., Lauritsen, K. B., Nielsen, J. K., and Syndergaard, S.: Evaluation of the 15-year ROM SAF monthly mean GPS radio occultation climate data record. Atmos. Meas. Technol. 13, 3081-3098, doi:10.5194/amt-13-3081-2020, 2020.

Gleisner, H., Ringer, M. A., and Healy, S. B.: Monitoring global climate change using GNSS radio occultation. npj Clim. Atmos. Sci. 5, 6, doi:10.1038/s41612-022-00229-7, 2022.

Ho, S. P., Anthes, R. A., Ao, C. O., Healy, S., Horanyi, A., Hunt, D., et al.: The COSMIC/FORMOSAT-3 radio occultation mission after 12 years: Accomplishments, remaining challenges, and potential impacts of COSMIC-2. Bull. Amer. Meteor. Soc., 101, E1107-E1136, doi:/10.1175/BAMS-D-18-0290.1, 2020.

Hong, T. X., Huang, C. Y., Lin, C. Y., Lien, G. Y., Huang, Z. M., and Chen, S. Y.: Impacts of GNSS RO Data on Typhoon Forecasts Using Global FV3GFS with GSI 4DEnVar. Atmosphere, 14, 735, doi:/10.3390/atmos14040735, 2023.

Hong, S. Y. and Lim, J. O. J.: The WRF single-moment 6-class microphysics scheme (WSM6). Asia-Pacific J. Atmos. Sci., 42, 460   129-151, 2006.

Hong, S. Y., Noh, Y. and Dudhia, J.: A new vertical diffusion package with an explicit treatment of entrainment processes. Mon. Wea. Rev., 134, 2318-2341, doi:/10.1175/MWR3199.1, 2006.

Hotta, D., Lonitz, K. and Healy, S.: Forward operator for polarimetric radio occultation measurements. Atmos. Meas. Tech., 17, 1075-1089, doi:/10.5194/amt-17-1075-2024, 2024.

465   Hristova-Veleva, S., Haddad, Z., Chau, A., Stiles, B. W., Turk, F. J., Li, P. P., et al.: Impact of microphysical parameterizations on simulated hurricanes—using multi-parameter satellite data to determine the particle size distributions that produce most realistic storms. Atmosphere, 12, 154., doi:/10.3390/atmos12020154, 2021.

Iacono, M. J., Delamere, J. S., Mlawer, E. J., Shephard, M. W., Clough, S. A., and Collins, W. D.: Radiative forcing by long-lived greenhouse gases: Calculations with the AER radiative transfer models. J. Geophys. Res. Atmos., 113, 470   doi:/10.1029/2008JD009944, 2008

Kain, J. S.: The Kain–Fritsch convective parameterization: an update. J. Appl. Meteorol. 43, 170-181, doi:/10.1175/1520-0450(2004)043<0170:TKCPAU>2.0.CO;2, 2004

Lien, G. Y., Lin, C. H., Huang, Z. M., Teng, W. H., Chen, J. H., Lin, C. C., et al.: Assimilation impact of early FORMOSAT-7/COSMIC-2 GNSS radio occultation data with Taiwan's CWB Global Forecast System. Mon. Wea. Rev., 149, 2171-475   2191., doi:/10.1175/MWR-D-20-0267.1, 2021.

Masson-Delmotte, V., Zhai, P., Pirani, A., Connors, S. L., Péan, C., Berger, S., et al.: Contribution of working group I to the sixth assessment report of the intergovernmental panel on climate change. Climate change. 2021.

Morrison, H., Thompson, G. and Tatarskii, V.: Impact of cloud microphysics on the development of trailing stratiform precipitation in a simulated squall line: Comparison of one-and two-moment schemes. Mon. Wea. Rev., 137, 991-480   1007, doi:/10.1175/2008MWR2556.1, 2009.

Murphy Jr, M. J., Haase, J. S., Padullés, R., Chen, S. H. and Morris, M. A.: The potential for discriminating microphysical processes in numerical weather forecasts using airborne polarimetric radio occultations. Remote Sens., 11, 2268, doi:/10.3390/rs11192268, 2019.

Padullés, R., Ao, C. O., Turk, F. J., de la Torre Juárez, M., Iijima, B., Wang, K. N. and Cardellach, E.: Calibration and 485   validation of the Polarimetric Radio Occultation and Heavy Precipitation experiment aboard the PAZ satellite. Atmos. Meas. Tech., 13, 1299-1313, doi:/10.5194/amt-13-1299-2020, 2020.

Padullés, R., Cardellach, E., Turk, F. J., Ao, C. O., de la Torre Juárez, M., Gong, J. and Wu, D. L.: Sensing horizontally oriented frozen particles with polarimetric radio occultations aboard PAZ: Validation using GMI coincident observations and Cloudsat a priori information. IEEE Trans. Geosci. Remote. Sens., 60, 1-13, 490   doi:/10.1109/TGRS.2021.3065119, 2022.

Padullés, R., Cardellach, E., Paz, A., Oliveras, S., Hunt, D. C., Sokolovskiy, S., et al.: The PAZ Polarimetric Radio Occultation Research Dataset for Scientific Applications. Earth Syst. Sci. Data Discuss, [preprint], doi:/10.5194/essd-2024-150, in review, 2024.

Ruston, B. and Healy, S.: Forecast impact of FORMOSAT-7/COSMIC-2 GNSS radio occultation measurements. Atmos. Sci. Lett., 22, e1019, doi:/10.1002/asl.1019, 2021.

Skamarock, W. C., Klemp, J. B., Dudhia, J., Gill, D. O., Liu, Z., Berner, J., et al.: A Description of the Advanced Research WRF Model Version 4.3(No. NCAR/TN-556+STR), doi:/10.5065/1dfh-6p97, 2021.

Tabari, H.: Climate change impact on flood and extreme precipitation increases with water availability. Sci. Rep., 10, 13768, doi:/10.1038/s41598-020-70816-2, 2020.

Talpe, M. J., Nguyen, V.A. and Tomás-Martínez, S.: Initial Polarimetric Radio Occultation Results from Spire's Nanosatellite Constellation: Satellite Payload, Collection and Calibration. Bull. Amer. Meteor. Soc., under review, 2024.

Tao, W. K., Simpson, J. and McCumber, M.: An ice-water saturation adjustment. Mon. Wea. Rev., 117, 231-235, doi:/10.1175/1520-0493(1989)117<0231:AIWSA>2.0.CO;2, 1989.

Tao, W. K., Wu, D., Lang, S., Chern, J. D., Peters-Lidard, C., Fridlind, A. and Matsui, T.: High-resolution NU-WRF simulations of a deep convective-precipitation system during MC3E: Further improvements and comparisons between Goddard microphysics schemes and observations. J. Geophys. Res. Atmos., 121, 1278-1305, doi:/10.1002/2015JD023986, 2016.

Thompson, G., Field, P. R., Rasmussen, R. M., and Hall, W. D.: Explicit forecasts of winter precipitation using an improved bulk microphysics scheme. Part II: Implementation of a new snow parameterization. Mon. Wea. Rev., 136(12), 5095-5115, doi:/10.1175/2008MWR2387.1, 2008.

Turk, F. J., Cardellach, E., de la Torre-Juárez, M., Padullés, R., Wang, K. N., Ao, C. O., et al: Advances in the Use of Global Navigation Satellite System Polarimetric Radio Occultation Measurements for NWP and Weather Applications. Bull. Amer. Meteor. Soc., 105, E905-E914, doi:/10.1175/BAMS-D-24-0050.1, 2024.